Metal-Organic-Framework-Derived Porous Carbon Embedded with TiO_2 Nanoparticles as a Cathode for Advanced Lithium–Sulfur Batteries

Chu Qi[+],[a] Huilan Li[+],[a] Jia Wang,[a] Chengcheng Zhao,[a] Cuimei Fu,[a] Lina Wang,*[a] and Tianxi Liu*[a, b]

The undesired internal shuttling of soluble polysulfide intermediates (Li_2S_n, $2 < n \leq 8$) remains the primary challenge hindering the development of lithium-sulfur (Li–S) batteries. Engineering and functionalizing the cathode structure to trap Li_2S_n is a straightforward approach to address this issue. Metal-organic framework (MOF)-derived materials are applausive candidate host materials of sulfur, owing to the highly porous characteristic. In this work, a Ti–MOF-derived micro-sized cake-like carbon skeleton with in situ generated hierarchical pores and anatase TiO_2 crystalline grains is applied as an effective sulfur host in Li–S batteries. In this rational design, the pyrolytic porous carbon provides fast ion diffusion and physical confinement of polysulfides. The polar TiO_2 affords abundant anchoring sites to achieve chemical encapsulation of sulfur species and accelerate polysulfide conversion kinetics. Benefiting from the fast reaction kinetics, the hybrid sulfur cathode delivers an elevated cycling performance with a capacity decay of only 0.39% per cycle at 0.5 C (1 C = 1675 mA g^{-1}) over 100 cycles. In addition, an improved rate capability of 620 mAh g^{-1} at 2 °C is obtained. This work affords a facile method to design optimized cathodes towards advanced Li–S batteries.

1. Introduction

The rechargeable batteries are approaching a bottleneck mainly due to the limited capacity of traditional cathodes based on the transition metal intercalation compounds.[1,2] The naturally abundant elemental sulfur (S_8) has drawn wide attention as one of the most promising candidate cathode material, which delivers a high specific capacity (1675 mAh g^{-1}) and energy density (2600 Wh kg^{-1}).[3,4] Despite these superiorities, the intrinsic insulation nature of sulfur and discharge products of Li_2S induces the sluggish redox reaction and poor ion diffusion.[5–7] Upon the conversion of $S_8 \rightarrow Li_2S$, the cathode suffers from a 70–80% volume expansion.[8,9] Besides, the notorious shuttle effect aroused by the diffusion of soluble intermediate polysulfides (Li_2S_n, $2 < n \leq 8$) leads to severe loss of sulfur and corrosion of Li-metal anode surface, which deteriorates the cyclic life of Li-S batteries.[10–12]

To address these challenges, diverse designs of cathode hosts have been intensively studied.[13,14] Among which, porous carbon materials that offer a physical confinement of polysulfides are the most widely developed.[15–17] In spite of highly improved conductivity of cathodes, the nonpolar surface of carbon makes it less effective to block the shuttle effect of the polar polysulfides. Metal-organic frameworks (MOFs) that composed of metal ions and organic ligands have a large variable pore structure.[18–21] Upon high-temperature pyrolysis, MOF-derived carbons are possible to retain the morphology of the MOFs. The metallic ions might be reduced to metal or metallic oxides, among which that with a polar surface that might act as chemical anchoring sites to trap Li_2S_n. Therefore, MOFs have been applied as templates of carbonaceous composites for Li-S batteries. For instance, Mai et al. employed the uniformly dispersed ZnO in MOF-derived carbon as the metal resource to in-situ synthesis a new ZIF-8 layer, showing the improved intimacy with polysulfides.[22] Lu et al. reported a ZIF-67-derived carbon nanocage embedded with Co nanoparticles.[23] Zhang et al. developed a jujube pit-like Fe_3O_4/C composite through the pyrolization of a Fe-based MOF.[24] De et al. used an Mg/MgO-embedded carbon as sulfur immobilizer from Mg-1,4-benzenedicarboxylate MOFs.[25]

The battery performance and sulfur loading amount are depended on the microstructure and properties of the MOF-derived carbons. A hierarchical porous structure and abundant chemisorption sites are preferred for strong physisorption and chemisorption to trap polysulfides. Among various polar compounds, titanium dioxide (TiO_2) has been proven to be particularly promising for its strong interactions with Li_2S_n.[26–28]

[a] C. Qi,[+] H. Li,[+] J. Wang, C. Zhao, Dr. C. Fu, Prof. L. Wang, Prof. T. Liu
State Key Laboratory for Modification of
Chemical Fibers and Polymer Materials
College of Materials Science and Engineering
Innovation Center for Textile Science and Technology
Donghua University
Shanghai 201620 (PR China)
E-mail: linawang@dhu.edu.cn
txliu@dhu.edu.cn
[b] Prof. T. Liu
Key Laboratory of Synthetic and Biological Colloids
Ministry of Education
School of Chemical and Material Engineering
Jiangnan University
Wuxi 214122 (PR China)
[+] These authors contributed equally to this work.

Supporting information for this article is available on the WWW under https://doi.org/10.1002/celc.202001122

Herein, a TiO_2/C composite with an uniform micro-sized pie-like morphology is prepared via one-step pyrolysis process of a titanium-containing MOF of MIL-125(Ti). The as-prepared TiO_2/C composite inherits the porous structure from the parent MIL-125(Ti). And additional micropores and mesopores are formed during carbonization due to the gas activation, which can provide abundant space for sulfur accommodation and facilitate electrolyte access for fast transportation of ions. Meanwhile, the porous skeleton can be directly functionalized by the in-situ generated highly ordered TiO_2 crystalline grains. Such a unique structure guarantees a high sulfur loading above 70 wt% and an effective sulfur utilization. As a result, the TiO_2/C–S cathode could effectively mitigate the shuttle of polysulfides to show an improved cycling performance of 100 cycles at 0.5 C (1 C = 1675 mA g^{-1}) with a capacity retention of 61%. Besides, a decent rate capability is achieved with a capacity of 619.6 mAh g^{-1} under a high current density of 2 C.

2. Results and Discussion

2.1. Synthesis and Characterization

The synthetic procedure of the Ti-MOF derived TiO_2/C composite is illustrated in Figure 1a. Firstly, a well-defined pie-like Ti-based titanium-p-phthalic acid MOF, namely MIL-125(Ti) ($Ti_8O_8(OH)_4(BDC)_6$, BDC = 1,4-benzene dicarboxylate), was prepared via a facile solvothermal method. The crystalline structure of the as-synthesized Ti-MOF is confirmed by the X-ray diffractometer (XRD) (Figure S1a). The visible diffraction peaks can be well indexed to a space group of *I4/mmm* (n° 139), corresponding to the MIL-125(Ti) crystals with an open porous structure (Figure S1b). According to the thermogravimetry (TG) analysis of MIL-125(Ti) upon heating under argon atmosphere (Figure S2), the TiO_2/C composite was then prepared from a pyrolysis process of MIL-125(Ti) at 800 °C. The sulfur was finally impregnated into the TiO_2/C to achieve the composite cathode of TiO_2/C–S.

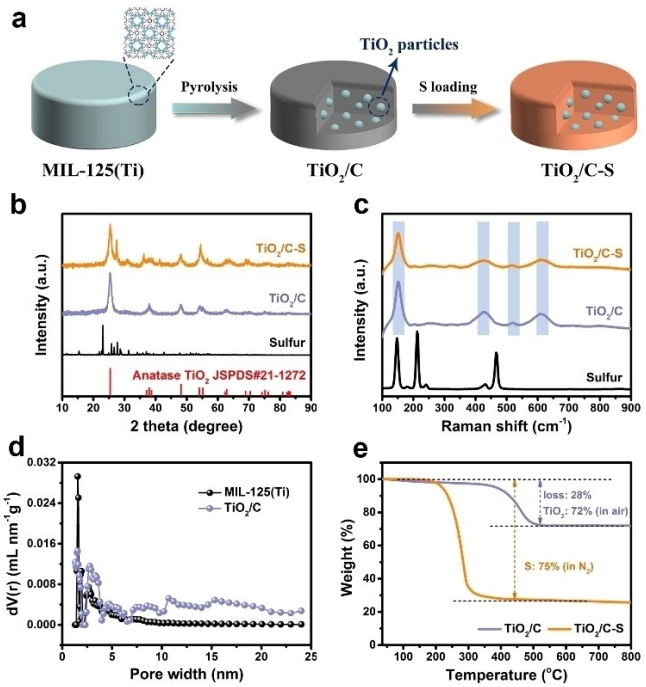

Figure 1. a) Schematic illustration for the fabrication of TiO_2/C–S. b) XRD patterns of TiO_2/C, TiO_2/C–S and S. c) Raman spectra of TiO_2/C and TiO_2/C–S. d) The nitrogen adsorption-desorption of TiO_2/C and TiO_2/C–S. e) TGA curves of TiO_2/C–S under Ar atmosphere and TiO_2/C under air atmosphere.

The XRD pattern of TiO_2/C suggests the typical anatase structure of TiO_2 (Figure 1b), identified by the standard card (JCPDS No. 21-1272). Compared with that of pristine elemental sulfur, the diffraction peaks attributed to sulfur become weak of TiO_2/C–S, indicating the uniform immobilization of sulfur in the TiO_2/C host.[29] The Raman spectra further confirms the composition of TiO_2 and sulfur in the TiO_2/C–S composite (Figure 1c). The sharp peak at 145 cm^{-1} in both TiO_2/C and TiO_2/C–S is the fundamental vibration mode of anatase titanium dioxide. The other peaks appear associated with TiO_2 are also observed at 423, 515 and 611 cm^{-1}.[30] The signals of sulfur are almost invisible in the spectrum of TiO_2/C–S, indicating there is no aggregation of sulfur species on the surface of TiO_2/C. To further explore the porous structure and specific surface area of the TiO_2/C composites, N_2 adsorption-desorption isotherms and the pore size distribution analysis were carried out. In spite that the Brunauer-Emmett-Teller (BET) surface area of TiO_2/C (231.3 $m^2 g^{-1}$) is reduced compared with the much highly porous parent MIL-125(Ti) (1386.1 $m^2 g^{-1}$), the hierarchical pore structure of TiO_2/C is proved by the obvious hysteresis loop in the range P/P_0 of 0.5–1.0 (Figure S3). The type H_4 hysteresis loop indicates the coexistence of micropores and mesopores.[31] The pore-size distribution analysis provides more evidence of the additional formed mesopores during pyrolysis of MIL-125 (Ti) (Figure 1d). After the impregnation of sulfur, the surface area of TiO_2/C–S distinctly decreased to 8.2 $m^2 g^{-1}$, which confirmed that the most nanopores in TiO_2/C are occupied by sulfur. The content of TiO_2 in TiO_2/C is 72 wt%, as calculated by thermogravimetric analysis (TGA) of the sample under air atmosphere (Figure 1e). And the TGA measurement of TiO_2/C–S under N_2 atmosphere shows a high sulfur content of 75 wt%.

The morphology of materials was investigated by field-emission scanning electron microscopy (FESEM) and transmission electron microscopy (TEM). Figure 2a and b shows that the uniform pan-like MIL-125(Ti) particles with a narrow size distribution ca. 1.5 μm. The surface of the particles is quite smooth (Figure 2c and Figure S4). After pyrolysis, the obtained TiO_2/C could reserve the uniform pan-like morphology (Figure 2d and e). However, compared with MIL-125(Ti), the TiO_2/C particles show obvious size shrinkage (~1.0 μm) and the surface appears much punky (Figure 2f). The change of the microstructure should be due to the gas activation from the decomposition of the oxygenic and hydric ligand during the pyrolysis. The TEM images reveal that the TiO_2 nanoparticles are well embedded in the carbon matrix (Figure 2g and h). The high-resolution TEM image further reveals the interlayer distance of 0.35 nm corresponding to the (101) lattice spacing of crystalline TiO_2 (Figure 2i).[32] The morphology of TiO_2/C–S is similar to that of TiO_2/C and no bulky sulfur is observed on the

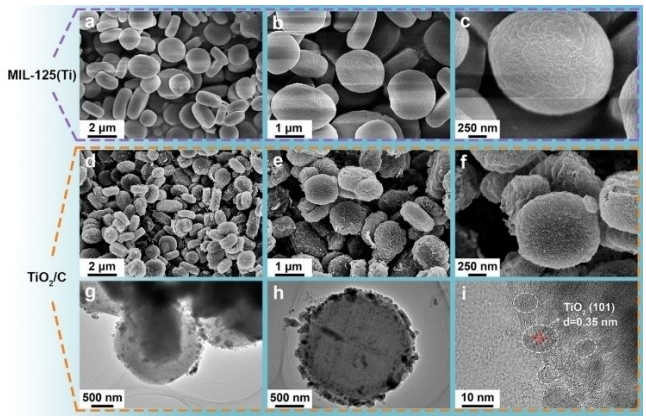

Figure 2. SEM images of (a–c) MIL-125(Ti) and (d–f) TiO_2/C. (g, h) TEM images and (i) HRTEM image of TiO_2/C.

surface (Figure 3a-c). The TEM element mappings of TiO_2/C–S depicted in Figure 3d further illustrate the homogenous distribution of C, O, Ti and S in the TiO_2/C–S particles.

2.2. Interactions between Li_2S_n and TiO_2/C Composites

To evaluate the interactions of TiO_2/C with polysulfides, the adsorption experiment by adding TiO_2/C powders into the Li_2S_6 solution (5 mM) was conducted. The color of the polysulfide solution changed from dark brown to transparent quickly (Inset in Figure 3e). The chemical states of the Li_2S_6 solution before and after adding TiO_2/C were analyzed by UV-vis absorption spectroscopy (Figure 3e). The remarkably decreased characteristic peaks corresponding to S_8^{2-}/S_6^{2-} and S_6^{2-}/S_4^{2-} at 225 and 280 nm further prove the strong chemical interactions between TiO_2/C and Li_2S_6. X-ray photoelectron spectroscopy (XPS) provides the underlying adsorption principles. The XPS survey spectra of TiO_2/C before and after adsorption of Li_2S_6 are demonstrated in Figure S5a. The existence of S element indicates the successful introduction of sulfur species in TiO_2/C after adsorption of Li_2S_6.[33]

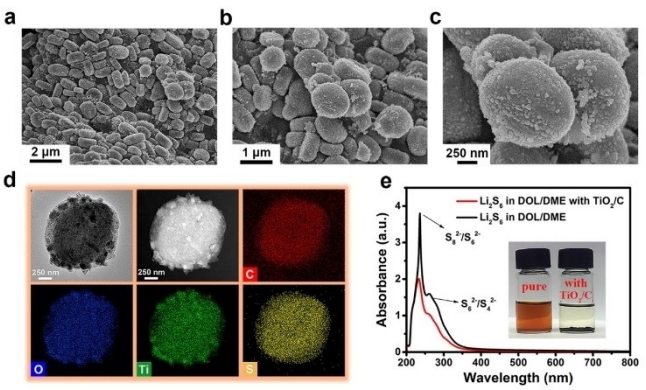

Figure 3. a–c) SEM images and d) elemental mapping of TiO_2/C–S. e) UV/Vis spectra and digital images (inset) of Li_2S_6 solution with and without TiO_2/C.

The Ti 2p spectrum shows two predominant peaks at 465.0 eV and 459.2 eV, which are assigned to Ti $2p_{1/2}$ and Ti $2p_{3/2}$, respectively (Figure S5b). The splitting data between the Ti $2p_{1/2}$ and Ti $2p_{3/2}$ core levels are 5.8 eV, indicating a normal state of Ti^{4+} in the anatase TiO_2.[34] The Ti 2p peaks after adsorption of Li_2S_6 show a shift of ca. 0.2 eV toward higher binding energy. And the peak at 465.2 eV is related to the Ti–S bond in titanium oxysulfide (TiOS) phase,[35] Figure S5c shows two doublets in S 2p spectrum, which are divided into four sulfur environments. The binding values of 164.8 and 164.3 eV are ascribed to bridging and terminal sulfur atoms. Strong signals in the higher binding energy area (170.2 and 169.3 eV) are associated with the sulfur species at higher oxidation state (sulfate), which arises from the interaction between Li_2S_6 and TiO_2/C.[36] In addition, an additional peak at 532.4 eV in O 1s spectrum after adsorption further proves the presence of sulfate and the other peak at 530.7 eV corresponds to the Ti–O–Ti bond (Figure S5d). Therefore, the capture ability of TiO_2/C towards polysulfides is supported by chemical Ti–S bond and sulfate, indicating the great potential for suppressing shuttle effect in Li–S cell.

2.3. Li^+ Storage Performance and Reaction Kinetics

To evaluate the electrochemical performance of TiO_2/C–S cathode, CR2025-type coin cells with a Li-metal anode were assembled. The sulfur loading is ca. 2 mg cm^{-2}. Cyclic voltammetry (CV) profiles of TiO_2/C–S and pristine sulfur cathode in the fifth cycle at 0.1 mV s^{-1} are shown in Figure 4a. Both of the cells present two cathodic peaks and an anodic peak, in accord with the typical multistep redox lithiation/delithiation processes of sulfur. For TiO_2/C–S cathode, the peaks located in 2.28 and 2.01 V associate with the conversion of circular sulfur to soluble long-chain Li_2S_n ($4 \le n \le 8$) and further reduction to insoluble Li_2S_2 and Li_2S respectively, while the peak at 2.40 V is related to the consecutive oxidation of low-order S_n^{2-} to S_8. The TiO_2/C–S cathode exhibits smaller peak position shifts and higher peak current compared with the pristine sulfur cathode, suggesting lower electrochemical polarization and improved reaction kinetics. Moreover, the initial CV cycles of TiO_2/C–S cathode show the highly overlapped peaks except for the first cycle irreversibility, implying stable electrochemical performance of the TiO_2/C–S cathode (Figure S6). In a similar manner to CV curves, the galvanostatic charge-discharge profiles of Li–S cells exhibit the typical two-plateau feature (Figure 4b and c). In comparison, TiO_2/C–S cathode delivers a higher initial coulombic efficiency of 97.4% than that of C–S cathode (92.9%) at a current density of 0.5 C (1 C = 1675 mA g^{-1}). Meanwhile, the lower discharge plateau that contributes majority of specific capacity remains in the similar voltage range, indicating the stable and rapid reaction dynamics. Especially, TiO_2/C–S cathode shows a much smaller overvoltage (△E, the potential gaps between discharge and charge curves), implying a rapid reaction kinetics at high current density. In terms of the cycling performance, the TiO_2/C–S cathode delivers a higher initial specific discharge capacity of 1281.4 mAh g^{-1} than that of pristine sulfur cathode (1141.4 mAh g^{-1}) at 0.5 C (Figure 4d). A

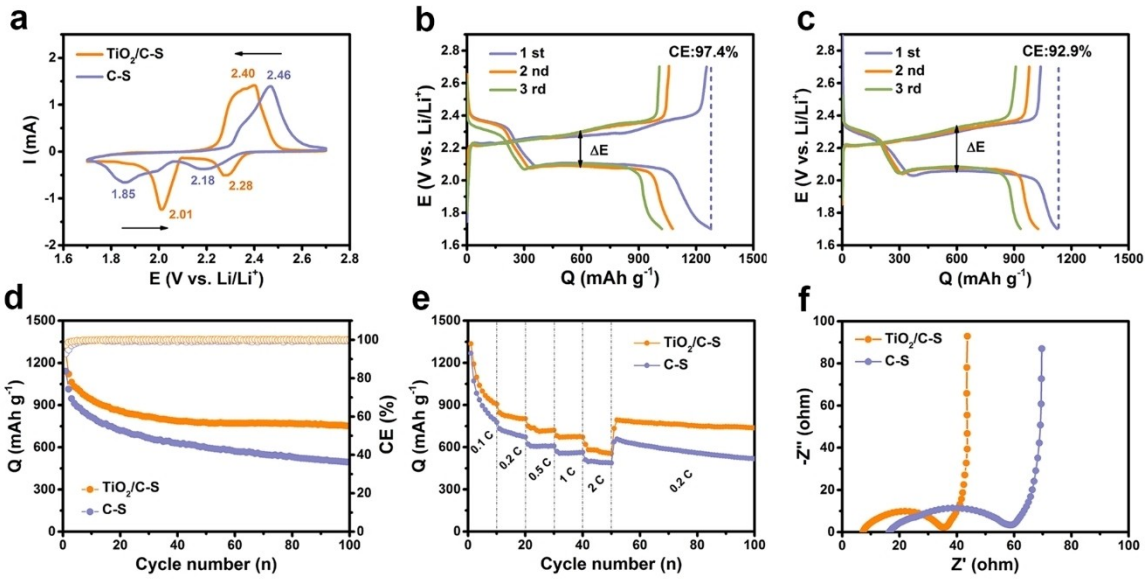

Figure 4. Electrochemical Characteristics of Li–S batteries with TiO_2/C–S and C–S cathode. a) CV curves upon the 5th cycle at 0.1 mV s^{-1}. The galvanostatic charge-ischarge profiles of b) TiO_2/C–S and c) C–S cathode at 0.5 C. d) Cyclic performance at 0.5 C. e) Rate capability. f) EIS profiles.

discharge capacity of 780.6 mAh g^{-1} with a small decay of 0.39% per cycle and a stable ca. 100% CE is obtained for TiO_2/C–S cathode. However, the sulfur cathode shows a severe capacity fade with a capacity retention of only 43.4%. In the voltage range of 1.7–2.7 V, the capacity contribution of TiO_2/C host can be negligible. As shown in Figure S7, it exhibits the initial capacity of 41.0 mAh g^{-1} and rapidly decays to 10 mAh g^{-1}. To further investigate the suppressed polysulfide shutting of the TiO_2/C–S cathode, the Li–S cells were disassembled after repeated cycles. Severe corrosion is observed on the cycled Li-anode surface with the C–S cathode (Figure S8a). Whereas, the cycled Li anode with the TiO_2/C–S cathode shows a much clean surface (Figure S8b), suggesting the effectively alleviated side reactions between Li_2S_n and Li metal. The rate capability at various current rates is shown in Figure 4e. In the case of TiO_2/C–S cathode, the discharge specific capacities at first cycle are 1336.2, 846.1, 749.8, 682.3, 619.6 mAh g^{-1} at 0.1, 0.2, 0.5, 1 and 2 C, respectively. However, only 510.5 mAh g^{-1} is displayed by the sulfur cathode at the high current density of 2 C.

The electrochemical impedance spectroscopy (EIS) was carried out to investigate the reaction kinetics of the Li–S cells. As depicted in Figure 4f, all the Nyquist plots displays a depressed semicircle in high-frequency region and a slant line in the low-frequency region, associated with the charge transfer resistant (R_{ct}) and Warburg impedance (Z_w), respectively. In contrast, the R_{ct} of the TiO_2/C–S cathode (28.1 Ω) is much smaller than that of the sulfur cathode (42.5 Ω). The Li^+ diffusion behavior was

further assessed to understand the effectiveness of TiO_2/C–S cathode in accelerating electrochemical reaction dynamics. Figure 5a and b shows the CV curves of TiO_2/C–S and pristine sulfur cathode under various scan rates from 0.05 to 0.5 mV s^{-1}. The corresponding linear fits between peak currents and the square root of sweep rates in one oxidation peak and a couple of reduction peaks are demonstrated in Figure 5c–e. Specifically, the Li^+ diffusion coefficient (D_{Li+}) is proportional to the slope of linear curves according to the Randles-Sevcik equation. As summarized in Table S1, the D_{Li+} is determined to be 9.14×10^{-9}, 1.82×10^{-9} and 2.45×10^{-9} cm^2 s^{-1} at peak O, R_1 and R_2 respectively for TiO_2/C–S cathode, which is larger than that of sulfur cathode. The improved utilization of active materials and polysulfide conversion kinetics should be resulted from the hierarchical porous structure of TiO_2/C–S and the abundant polar TiO_2 anchoring site. Benefit from the rational design, the cathode does not show obvious performance deterioration as the increase of sulfur loading to ca. 4 mg cm^{-2} (Figure S9).

3. Conclusions

In summary, we have fabricated a Ti–MOF derived hierarchically porous TiO_2/C composite as sulfur host, where abundant TiO_2 crystalline grains are homogenously embedded in the carbon matrix. The polar TiO_2 with hydrophilic groups (Ti–O) and surface hydroxyl groups can provide the chemical adsorption towards long-chain polysulfides, guaranteeing a high utilization of sulfur and accelerated polysulfide conversion kinetics. Simultaneously, the hierarchically porous structure provides abundant space for sulfur accommodation and facilitates electrolyte access for fast transportation of ions. Under the condition of TiO_2/C–S cathode, the Li–S cells exhibit the excellent cycling performance and rate capability with high reversible specific capacity. This work unfolds a great promise in the field of electrochemical energy storage materials.

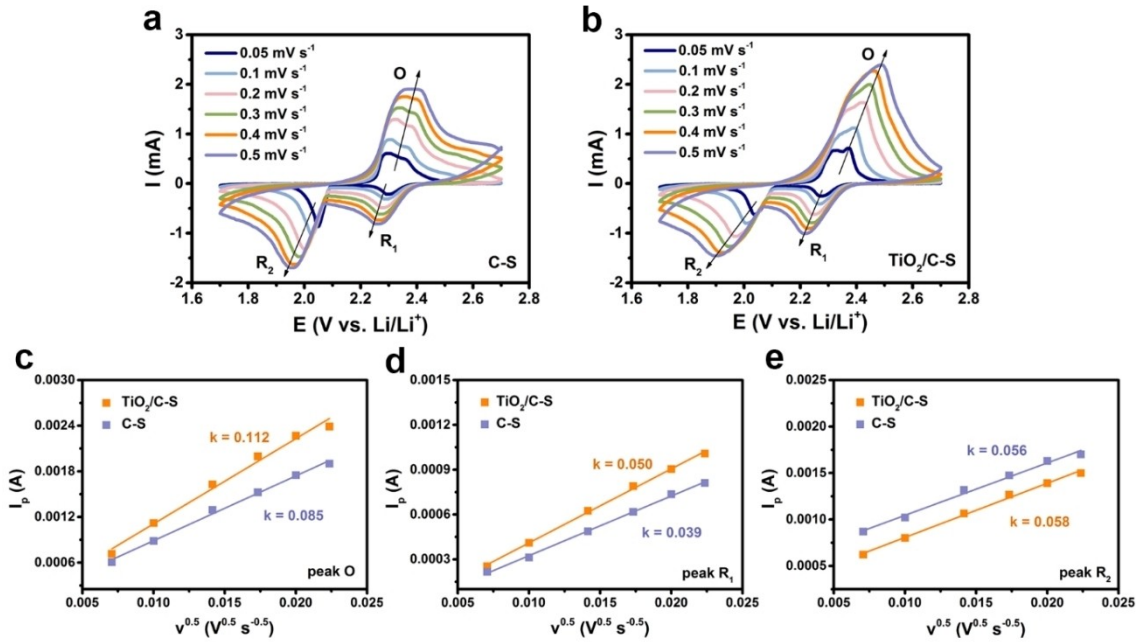

Figure 5. CV curves of a) C–S and b) TiO_2/C–S cathode at various scan rates from 0.05 to 0.5 mV s^{-1}. The Li^+ diffusion coefficients of C–S and TiO_2/C–S cathode at c) peak O, d) peak R_1 and e) peak R_2.

Experimental Section

Preparation of MIL-125(Ti)

MIL-125(Ti) was synthesized via a solvothermal process. In a typical synthesis, 3 g 1,4-benzenedicarboxylic acid (H_2BDC, Aladdin, 99%) was added into a mixture of 54 mL N, N-dimethylformamide (DMF, Sinopharm Chemical, ≥99.0%) and 6 mL anhydrous methanol (Sinopharm Chemical, ≥99.7%). Then, 1.56 mL tetra-n-butyl titanate $Ti(OC_4H_9)_4$ (Sigma-Aldrich, 97%) was added into the above solution with continuous stirring. The turbid mixture was transferred into a Teflon-lined autoclave after stirring for 4 h and heated up to 150 °C for 24 h subsequently. When cooled to the room temperature, the resulted product was washed with DMF and methanol and dried in vacuum oven at 60 °C to yield MIL-125(Ti) crystals.

Preparation of TiO_2/C

The as-synthesized MIL-125(Ti) was thermally treated at 300 °C for 4 h and then at 800 °C for 2 h to give the black TiO_2/C powder under argon protection.

Preparation of TiO_2/C-S

The mixture of TiO_2/C and the elemental sulfur (Sinopharm Chemical, chemical purity) with a weight ratio of 1:4 was heat-treated at 155 °C under an argon flow at a speed of 5 °C min^{-1} for 12 h, followed by 300 °C for 2 h to remove the extra sulfur. The resulted product was denoted as TiO_2/C–S.

Materials Characterization

X-ray diffraction (XRD) was carried out on an X-ray diffractometer with Cu Kα radiation (D/max-2550VB+/PC, Rigalcu). Raman spectra were obtained by an inVia Raman spectrometer system (Renishaw, UK). The morphology of the materials was investigated using field emission scanning electron microscopy (FESEM, JSM-7500F, JEOL) and transmission electron microscopy (TEM, JEM-2100F, JEOL). Thermal gravimetric analysis was conducted by thermogravimetry (TGA, NETZSCH 209 F1 Libra) at a heating rate of 10 °C min^{-1}. The nitrogen sorption/desorption measurements were conducted on a Quadrasorb adsorption instrument (ASIQMUOOUOO-6, Quantachrome). The apparent surface area and pore size distribution was calculated using the Brunauer-Emmett-Teller (BET) method and the nonlocal density functional theory (NLDFT) equilibrium model method, respectively.

Electrochemical Measurements

All of the materials used in the preparation of cathode were thoroughly dried before use. The sulfur cathode was prepared by casting the homogeneous slurry containing TiO_2/C–S, Ketjen Black (KB, ECP-600JD) and PVdF (10 wt% in NMP) with a weight ratio of 7:2:1 onto Al current collector. If not specially mentioned, the sulfur loading is ca. 2 mg cm^{-2}. A higher sulfur loading of ca. 4 mg cm^{-2} was tested as well. A pristine sulfur cathode with pure sulfur powder was also prepared in the same way as a control. Then, the obtained cathodes were cut into circular disks with a diameter of 12 mm. Polypropylene/polyethylene membrane (Celgard 2325) and Li metal foil was used as separator and anode. The electrolyte used was 1 M bis(trifluoromethane)sulfonimide lithium salt (LiTFSI) in 1,3-dioxolane (DOL) and dimethoxymethane (DME) (v/v = 1:1) with 0.2 M $LiNO_3$ additive. CR2025-type coin cells were assembled in an Ar-filled glove box (Mikrouna) for electrochemical evaluation. The electrolyte amount was controlled at ~20 μL in each cell.

The galvanostatic cycling was conducted in a fixed voltage range of 1.7–2.7 V on a NEWARE cell test system (Shenzhen, China). Electrochemical impedance spectroscopy (EIS) was performed on a CHI660E electrochemical workstation (Shanghai Chenhua, China) in the range of 0.01 Hz-1000 kHz. Cyclic voltammetry (CV) was carried

out on an Arbin workstation (Arbin Instruments, USA) in the potential range of 1.7–2.7 V (vs. Li/Li^+) at various sweep rates.

Lithium-ion diffusion coefficient D_{Li+} ($cm^2 s^{-1}$) was evaluated by cyclic voltammetry and calculated according to the Randles-Sevcik equation:[37]

$$I_p = 2.69 \times 10^5 n^{1.5} A D_{Li+}{}^{0.5} C_{Li} v^{0.5} \quad (1)$$

where I_p is the peak current, n represents the number of electrons (for Li–S batteries, $n = 2$), A indicates the electrode area, C_{Li} means the lithium-ion concentration in the electrolyte, and v stands for the scanning rate.

Acknowledgements

The authors gratefully acknowledge funding support from the Fundamental Research Funds for the Central Universities (2232018D3-02), and the Shanghai Scientific and Technological Innovation Project (18JC1410600).

Conflict of Interest

The authors declare no conflict of interest.

Keywords: Lithium-sulfur batteries · metal-organic framework · hierarchical porosity · shuttle effects · polysulfide conversion

[1] L. Yang, X. Zhu, X. Li, X. Zhao, K. Pei, W. You, X. Li, Y. Chen, C. Lin, R. Che, *Adv. Energy Mater.* **2019**, *9*, 1902174.
[2] G. Liang, L. Yang, Q. Han, G. Chen, C. Lin, Y. Chen, L. Luo, X. Liu, Y. Li, R. Che, *Adv. Energy Mater.* **2020**, *10*, 1904267.
[3] M. S. Whittingham, *Chem. Rev.* **2004**, *104*, 4271–4302.
[4] P. G. Bruce, S. A. Freunberger, L. J. Hardwick, J.-M. Tarascon, *Nat. Mater.* **2012**, *11*, 19–29.
[5] H. Li, X. Wang, C. Qi, C. Zhao, C. Fu, L. Wang, T. Liu, *Phys. Chem. Chem. Phys.* **2020**, *22*, 2157–2163.
[6] M. Zhao, H.-J. Peng, B.-Q. Li, X. Chen, J. Xie, X. Liu, Q. Zhang, J.-Q. Huang, *Angew. Chem. Int. Ed.* **2020**, *59*, 9011–9017.
[7] B.-Q. Li, L. Kong, C.-X. Zhao, Q. Jin, X. Chen, H.-J. Peng, J.-L. Qin, J.-X. Chen, H. Yuan, Q. Zhang, J.-Q. Huang, *Info. Mat.* **2019**, *1*, 533–541.
[8] L. Wang, Y. Zhao, M. L. Thomas, H. R. Byon, *Adv. Funct. Mater.* **2014**, *24*, 2248–2252.
[9] X. Wang, Y. Qian, L. Wang, H. Yang, H. Li, Y. Zhao, T. Liu, *Adv. Funct. Mater.* **2019**, *29*, 1902929.
[10] N.-S. Choi, Z. Chen, S. A. Freunberger, X. Ji, Y.-K. Sun, K. Amine, G. Yushin, L. F. Nazar, J. Cho, P. G. Bruce, *Angew. Chem. Int. Ed.* **2012**, *51*, 9994–10024; *Angew. Chem.* **2012**, *124*, 10134–10166.
[11] L. Wang, J. Liu, S. Yuan, Y. Wang, Y. Xia, *Energy Environ. Sci.* **2016**, *9*, 224–231.
[12] J. Wang, C. Fu, X. Wang, Y. Yao, M. Sun, L. Wang, T. Liu, *Electrochim. Acta* **2018**, *292*, 568–574.
[13] L. Qu, P. Liu, X. Tian, C. Shu, Y. Yi, P. Yang, T. Wang, B. Fang, M. Li, B. Yang, *ChemElectroChem* **2020**, *7*, 1679–1688.
[14] S.-J. Kim, M. Ahn, J. Park, Y. Jeoun, S.-H. Yu, D.-H. Min, Y.-E. Sung, *ChemElectroChem* **2020**, *7*, 3653–3655.
[15] J. Zhang, C.-P. Yang, Y.-X. Yin, L.-J. Wan, Y.-G. Guo, *Adv. Mater.* **2016**, *28*, 9539–9544.
[16] C. Zhang, H. B. Wu, C. Yuan, Z. Guo, X. W. Lou, *Angew. Chem. Int. Ed.* **2012**, *51*, 9592–9595; *Angew. Chem.* **2012**, *124*, 9730–9733.
[17] M. D. Patel, E. Cha, C. Kang, B. Gwalani, W. Choi, *Carbon* **2017**, *118*, 120–126.
[18] G. Li, H. Kobayashi, J. M. Taylor, R. Ikeda, Y. Kubota, K. Kato, M. Takata, T. Yamamoto, S. Toh, S. Matsumura, H. Kitagawa, *Nat. Mater.* **2014**, *13*, 802–806.
[19] Z. Xie, T. Li, N. L. Rosi, M. A. Carreon, *J. Mater. Chem. A* **2014**, *2*, 1239–1241.
[20] L. Jiao, Y. Wang, H. L. Jiang, Q. Xu, *Adv. Mater.* **2018**, *30*, 1703663.
[21] K. Suresh, A. J. Matzger, *Angew. Chem. Int. Ed.* **2019**, *58*, 16790–16794.
[22] T. Pan, Z. Li, Q. He, X. Xu, L. He, J. Meng, C. Zhou, Y. Zhao, L. Mai, *Energy Storage Mater.* **2019**, *23*, 55–61.
[23] D. Xiao, Q. Li, H. Zhang, Y. Ma, C. Lu, C. Chen, Y. Liu, S. Yuan, *J. Mater. Chem. A* **2017**, *5*, 24901–24908.
[24] L. Fan, H. Wu, X. Wu, M. Wang, J. Cheng, N. Zhang, Y. Feng, K. Sun, *Electrochim. Acta* **2019**, *295*, 444–451.
[25] T. Dhawa, S. Chattopadhyay, G. De, S. Mahanty, *ACS Omega* **2017**, *2*, 6481–6491.
[26] Z. Xiao, Z. Yang, L. Wang, H. Nie, M. Zhong, Q. Lai, X. Xu, L. Zhang, S. Huang, *Adv. Mater.* **2015**, *27*, 2891–2898.
[27] M. Yu, J. Ma, H. Song, A. Wang, F. Tian, Y. Wang, H. Qiu, R. Wang, *Energy Environ. Sci.* **2016**, *9*, 1495–1503.
[28] Z. W. Seh, W. Li, J. J. Cha, G. Zheng, Y. Yang, M. T. McDowell, P.-C. Hsu, Y. Cui, *Adv. Mater.* **2015**, *27*, 2891–2898.
[29] J. Li, B. Ding, G. Xu, L. Hou, X. Zhang, C. Yuan, *Nanoscale* **2013**, *5*, 5743–5746.
[30] M. Ocana, J. V. Garcia-Ramos, C. J. Serna, *J. Am. Ceram. Soc.* **1992**, *75*, 2010–2016.
[31] S. Evers, T. Yim, L. F. Nazar, *J. Phys. Chem. C* **2012**, *116*, 19653–19658.
[32] B. Qiu, M. Xing, J. Zhang, *J. Am. Chem. Soc.* **2014**, *136*, 5852–5855.
[33] T. Lei, Y. Xie, X. Wang, S. Miao, J. Xiong, C. Yan, *Small* **2017**, *13*, 1701013.
[34] Y. Luo, J. Luo, J. Jiang, W. Zhou, H. Yang, X. Qi, H. Zhang, H. J. Fan, D. Y. W. Yu, C. M. Li, T. Yu, *Energy Environ. Sci.* **2012**, *5*, 6559–6566.
[35] D. Gonbeau, C. Guimon, G. Pfister-Guillouzo, A. Levasseur, G. Meunier, R. Dormoy, *Surface Science* 1991, 254, 81–89.
[36] X. Liang, C. Hart, Q. Pang, A. Garsuch, T. Weiss, L. F. Nazar, *Nat. Commun.* **2015**, *6*, 5682.
[37] Z. A. Ghazi, X. He, A. M. Khattak, N. A. Khan, B. Liang, A. Iqbal, J. Wang, H. Sin, L. Li, Z. Tang, *Adv. Mater.* **2017**, *29*, 1606817.

Manuscript received: August 25, 2020
Revised manuscript received: September 11, 2020
Accepted manuscript online: September 22, 2020